Electronic Supplementary Material (ESI) for Journal of Materials Chemistry A.
This journal is © The Royal Society of Chemistry 2022

Boosting the Interfacial Hydrogen Migration for Efficient Alkaline Hydrogen Evolution on Pt-Based Nanowires

Wenchuan Lai,[1,I] Penglin Yu,[1,I] Lei Gao,[1] Zhilong Yang,[1] Bingling He,[2,*] and Hongwen Huang[1,3*]

[1] College of Materials Science and Engineering, Hunan University, Changsha, Hunan 410082, P. R. China.

[2] College of Physics and Electronic Engineering, Xinxiang University, Xinxiang, Henan 453003, P. R. China

[3] Shenzhen Research Institute of Hunan University, Shenzhen, Guangdong 518055, P. R. China

[I] These authors contributed equally to this work.

Correspondence and requests for materials should be addressed to B.H. (hbl626@126.com); H.H. (huanghw@hnu.edu.cn).

Abstract

The alkaline hydrogen evolution reaction (HER) on Pt-based catalysts is largely retarded by insufficient supply of dissociated hydrogen (*H) on Pt sites. Hydrogen spillover offers a promising solution to deliver the reactive *H, however, the hydrogen migration process generally suffers from thermodynamic/kinetic obstacles. Herein, we demonstrate that hydrogen spillover on binary PtNi nanowires can be thermodynamically and kinetically boosted by P-doping, resulting in the substantially improved alkaline HER. A combination of experimental and theoretical investigations suggests that the dual roles of incorporated P heteroatoms in facilitating the hydrogen spillover, involving the increased *H coverage *via* promoting the water dissociation, and the accelerated hydrogen migration across Pt-Ni interface to Pt sites *via* lowering kinetic barrier. Benefiting from the enhanced *H supply on Pt sites, the P-doped PtNi nanowires expressed an impressive alkaline HER performance (η_{10} 12 mV, mass activity 5.8 A mg^{-1}_{Pt} at 70 mV), outperforming most of state-of-the-art HER electrocatalysts.

Keywords: Hydrogen evolution reaction; interfacial hydrogen migration; Pt-based nanowires; P-doping; thermodynamics and kinetics

Introduction

Green hydrogen production from electrocatalytic water splitting has been considered as a promising method for effective transformation and utilization of sustainable energy sources so as to alleviate the global environmental problem and energy crisis.[1, 2] Rational design of robust electrocatalyst undertakes the central role on the route to deploying hydrogen evolution reaction (HER) technology.[3, 4] By far, Pt is supposed to be the top HER electrocatalyst with good intrinsic activity originated from its appropriate hydrogen adsorption Gibbs free energy (ΔG_H), according to the Sabatier principle.[5] Unfortunately in alkaline medium that is beneficial to anode protection during water electrolysis, the HER activity of Pt is 2~3 orders of magnitude lower than that in acid.[6] Given that the shortage of reactive protons in alkaline electrolyte and sluggish water dissociation ($* + H_2O + e^- \leftrightarrows *H + OH^-$, Volmer step) on Pt, the insufficient supply of dissociated hydrogen (*H) to Pt sites severely retards the alkaline HER kinetics.[7]

To address the issue, incorporating another promoter component, like the transition metal (TM, e.g., Ni, Fe, Co, etc.) or their oxides/hydroxides, into Pt matrix, can significantly boost the Volmer step in alkaline medium and increase *H for latter Heyrovsky/Tafel step.[8, 9] In the meantime, the alloying/hybridization strategy also enables to lower the usage of noble Pt material to reduce the catalyst cost. Despite the advances from such a binary design, the thorough consideration on *H delivery is still inadequate. Specifically, it is previously assumed that water dissociation reactions take place at Pt-TM interface, resulting in *OH and *H species binding with TM and Pt sites, respectively. However, in most practical cases, the interfacial phase should account for small percentage of bulk phase, for instance in the pioneering work of Markovic *et al.*, the lateral dimension of segregated Ni clusters deposited on Pt matrix ranges from 8 to 10 nm.[8] It is therefore hinted that in a phase-separated Pt-TM binary system, the water dissociation should mainly occur in inside region of TM phase, rather than the interfacial sites.[2, 10] In this case, the formed *H have to be transferred from TM phase to Pt phase in the first place, followed by the hydrogen combination and desorption on Pt sites.[11-13]

In this regard, hydrogen spillover is recently focused that offers new insights to enhance the

*H supply and HER activity of binary catalysts.[12, 14-17] The hydrogen spillover typically proceeds through hydrogen migration from H-enriched sites (also strong *H adsorption sites) to H-deficient sites (also weak *H adsorption sites), similar to the case of abovementioned binary system.[15, 18] Interestingly, due to the moderate ΔG_H on Pt sites close to thermo-neutral point, Pt can act as *H donating sites or accepting sites, depending on the *H binding strength of secondary component.[10, 13, 19-21] Although hydrogen spillover is first discovered in acidic HER system, up-to-date researches also witness the spillover behavior in alkaline HER, which is meaningful to strengthen the *H supply for Pt-based binary catalyst in alkali.[10, 12, 22, 23] It must be pointed out that, because hydrogen spillover from strong to weak *H sites is intrinsically unfavorable in thermodynamics, it will inevitably require the adequate driving force.[18] On the other hand, the hydrogen spillover across the interfaces, has to overcome the high migration kinetic barriers.[15] These two challenges could give rise to the less-motivated or even frustrated hydrogen spillover on binary catalysts under HER conditions. Consequently, the manipulation on interfacial migration of *H is of particular importance to optimize the catalytic activity. To this end, some previous works showcase the potential impacts of catalyst structure (like particle size[24] or crystalline phase[10]) and ligand modification[18], on hydrogen spillover process. However, the strategy to thermodynamically and kinetically accelerate interfacial hydrogen migration, is still insufficient to date for Pt-based binary catalysts, hindering the further improvement of alkaline HER activity.

Doping with metalloid element has proved to be an efficient strategy to improve the intrinsic activity of electrocatalysts, where phosphorus (P) with abundant valence electrons shows great potential on reshaping the electronic structure and optimizing the adsorption energy of key reaction species.[25, 26] Herein, we demonstrated that P-doping can boost interfacial hydrogen spillover on Pt-based binary catalyst so as to increase *H supply on Pt sites for efficient alkaline HER. Through a wet-chemical method, we have synthesized ultrafine binary PtNi nanowires (PtNi NWs), and then realized P incorporation by vapor phase annealing method. Theoretical simulations together with experimental evidences confirmed the effect of P

heteroatoms on optimizing electronic structures of PtNi catalyst, leading to the improved thermodynamics and kinetics driving force for hydrogen migration, from Ni sites to Pt sites, under HER conditions. As consequences of the enhanced *H supply, the P-doped nanowires (PtNiP NWs) delivered an impressive alkaline HER performance, markedly outperforming the bench mark Pt/C and most of state-of-the-art electrocatalysts. This work demonstrates the availability of hydrogen spillover in promoting alkaline HER, and can enlighten the reasonable design of catalysts by manipulating *H delivery.

Results and discussion

Synthesis and structural characterizations of P-doped PtNi NWs

In a typical synthesis displayed as Fig. 1a, ultrafine PtNi NWs were firstly prepared through wet-chemical route from Pt and Ni precursors (see Experimental methods for details). Fig. 1b presents the low-magnification transmission electron microscopy (TEM) image of as-prepared PtNi NWs, where ultrafine nanowires with shish-kebab-like features can be clearly observed. The statistical analysis manifests an average length at around 60 nm for PtNi NWs, and an average diameter of 6.5 nm in protuberance position (Fig. 1b inset). In the following P-doping process, the as-prepared PtNi NWs were loaded on carbon supports in advance to avoid the aggregation, and then heated at 250 °C for 2 h with $NaH_2PO_4 \cdot H_2O$ as phosphorus source. The P-doped nanowires (PtNiP NWs) were finally labeled as PtNiP-0.03 NWs, PtNiP-0.11 NWs and PtNiP-0.81 NWs respectively, based on the P/Pt atomic ratio determined by inductively coupled plasma-atomic emission spectroscopy (ICP-AES) shown in Table S1. It should be noted that the as-prepared PtNi NWs hold a Ni/Pt atomic ratio of 1.89, while the heat treatment even in the absence of phosphorus source, still lessens the Ni/Pt ratio (e.g., 1.11 for PtNi NWs). The difference hints that thermal treatment caused Ni emigration and loss, while meantime some Ni segregations could exist in PtNiP NWs.[27, 28]

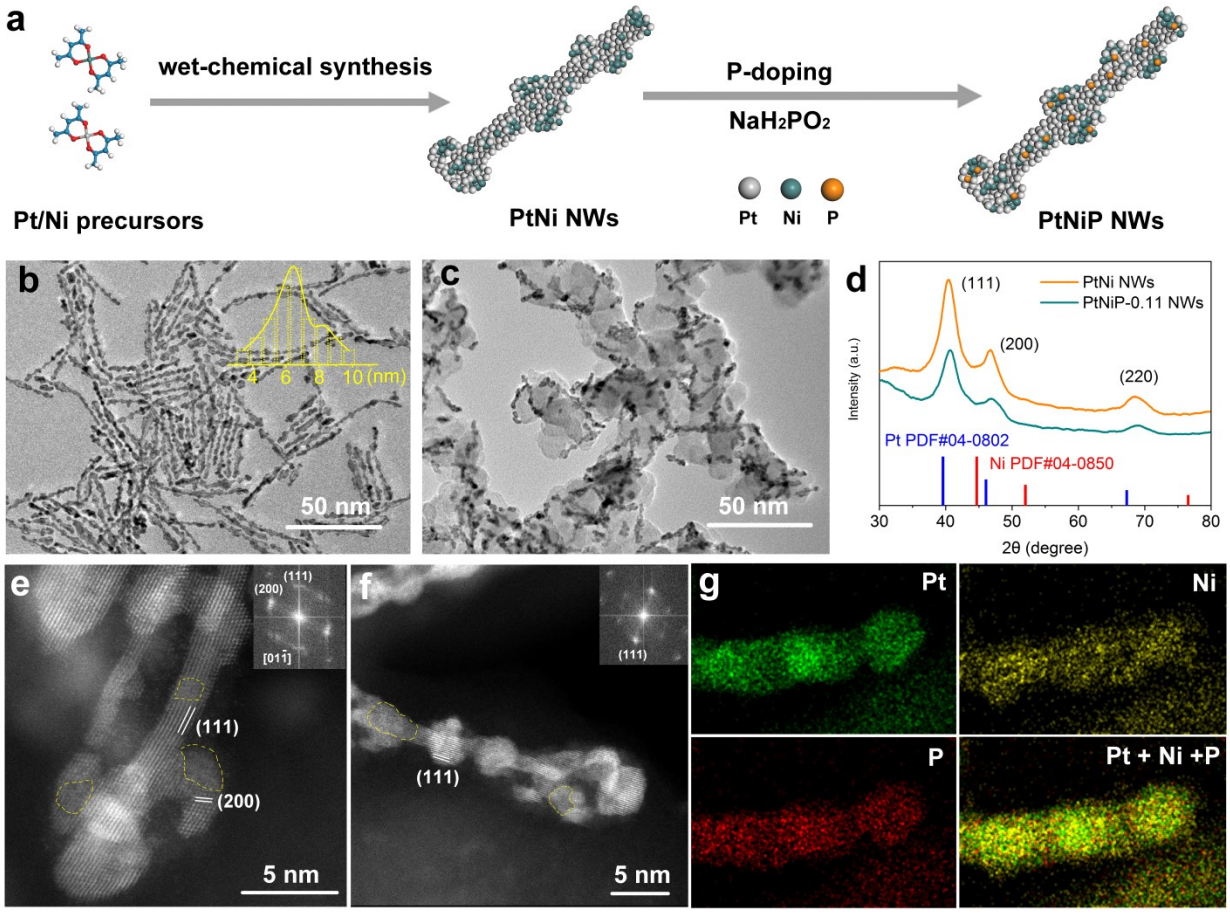

Fig. 1 Structural characterizations of as-prepared PtNi NWs and PtNiP NWs. (a) Preparation method of PtNiP NWs comprised of wet-chemical synthesis and P-doping step. (b) Low-magnification TEM image of PtNi NWs before P-doping. The inset is the diameter distribution of nanowires (average diameter at around 6.5 nm). (c) Low-magnification TEM image of PtNiP-0.11 NWs after P-doping. (d) XRD patterns of PtNi NWs and PtNiP-0.11 NWs. (e) and (f) Atomic-resolution aberration-corrected HAADF-STEM images of PtNiP-0.11 NWs. The insets correspond to the FFT patterns. The regions encircled by yellow dashed lines correspond to amorphous segregational Ni clusters. (g) EDS mapping along a PtNiP-0.11 NWs including Pt, Ni, P elements and overlapping.

Fig. 1c, S1 and S2 exhibit the low-magnification images of several PtNiP NWs, in which the nanowires structures with some protuberances are basically remained in PtNiP-0.03 NWs and

PtNiP-0.11 NWs, with slight decrease in axial length. Note that P-doping under high temperature also created some hollow features inside the nanowires beneficial to the exposure of active sites. By contrast, PtNiP-0.81 NWs has mostly been broken into small particles, probably arisen from the too drastic phosphorization reaction. The X-ray diffraction (XRD) pattern of PtNi NWs in Fig. 1d shows the typical face-centered cubic (*fcc*) structural features of PtNi nanowires with some right shift compared to pure Pt, which is caused by the incorporation of Ni atoms. After P-doping, the XRD characteristic is slightly changed for PtNiP NWs (Fig. S3), indicating no drastic transformation in crystalline structure after mild P-doping and the formation of some amorphous structures probably associated with segregational Ni cluster. This further echoes with the XRD pattern of excessively P-doped PtNiP-0.81 NWs where much more amorphous structures can be observed. Moreover, high-angle annular dark-field scanning transmission electron microscopy (HAADF-STEM) was collected to determine the microstructure and atomic packing of PtNiP-0.11 NWs. The nanowire characteristic with some protuberances and hollow positions was further confirmed (Fig. S4). By measuring the lattice parameters, we distinguish the fringes matching with (111) and (200) planes of typical *fcc* PtNi alloys, in line with the fast Fourier transform (FFT) pattern displayed in the insets (Fig. 1e-1f).[29, 30] Meanwhile, we also notice some amorphous region in atomic-resolution HAADF-STEM images (encircled by yellow dashed lines in Fig. 1e-1f), which further confirms the existence of amorphous segregational Ni clusters, in line with the hints from ICP-AES and XRD.

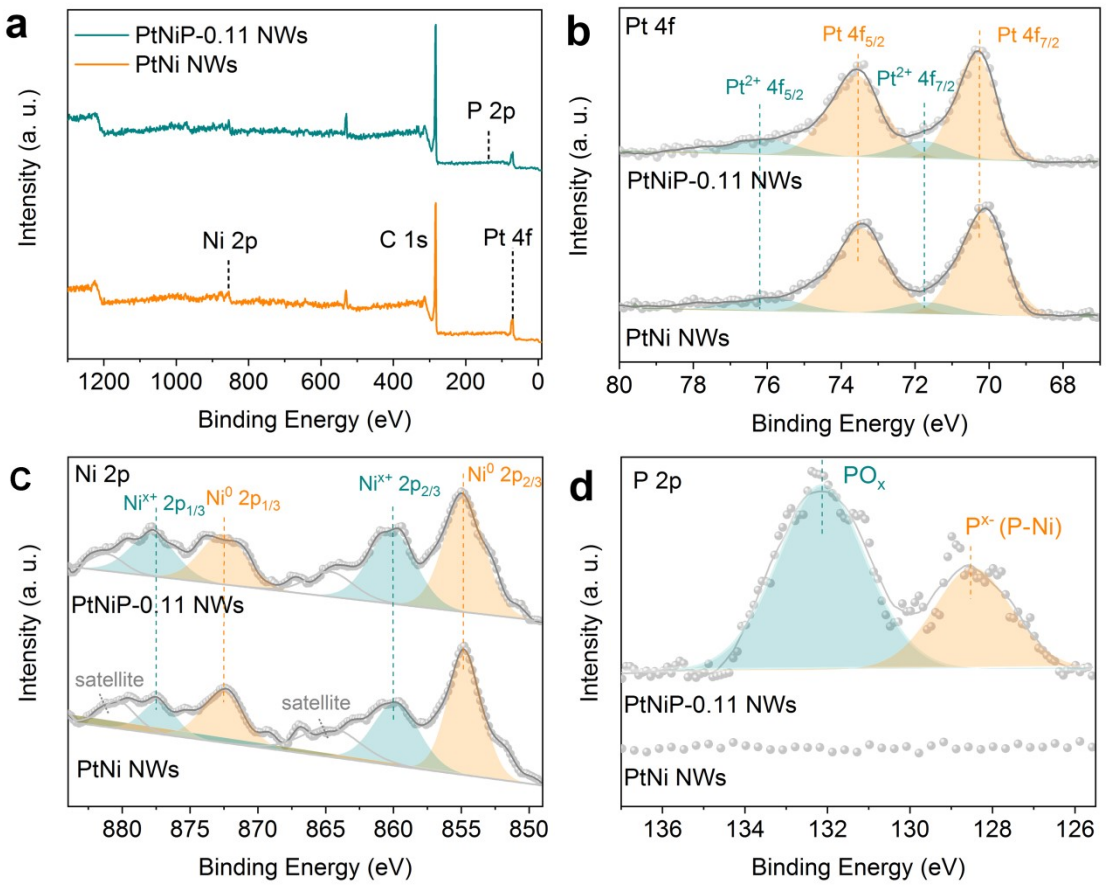

Fig. 2 XPS spectra comparison between PtNi NWs and PtNiP-0.11 NWs. (a) Survey spectra. (b)-(d) Pt 4f, Ni 2p, and P 2p spectra, respectively.

Chemical composition was then analyzed based on energy dispersive spectroscopy (EDS) elemental mapping profile. As Fig. 1g and S5 reveal, the doped P element homogeneously distribute throughout the whole PtNiP-0.11 NWs. On the other hand, X-ray photoelectron spectroscopy (XPS) was collected to monitor the evolution in chemical environment of nanowire after P-doping (Fig. 2). To offset the effect of high temperature, here we adopt the PtNi NWs after heat treatment under N_2 atmosphere, instead of as-prepared nanowires, as a contrast sample (TEM shown in Fig. S6). The Pt 4f and Ni 2p spectra typically contain metallic and oxidized states for both PtNi NWs and PtNiP-0.11 NWs (Fig. 2b and 2c), where oxidized Ni could appears as NiO or $Ni(OH)_2$ species. Notably, the Ni^{x+}/Ni^0 and Pt^{2+}/Pt^0 ratio increase from 0.55 to 0.74 and from 0.18 to 0.23 respectively, which could be traced to the charge transfer interaction

between metal and P atoms. Besides, from spectrum in Fig. 2d, P element mainly appears as P^{x-} (mainly bonding with Ni, 128.6 eV) and PO_x (result of surface oxidation by air, 128.6 eV) state,[31-33] while the evident negative shift of peak P^{x-} relative to pure P (130.4 eV) again implies the electron transfer from metal to P atoms.[34] Therefore, all these results support the uniform P-doping on PtNiP-0.11 NWs without markedly affecting nanowire morphologies, and the electronic structure could be modulated meantime enabling the alteration of catalytic behaviors.

Evaluation of alkaline HER performance

To investigate the P-doping effect on the catalytic performance, we then evaluated the HER performance by a three-electrode system in N_2-saturated 1 M KOH. As references, PtNi NWs (after heat treatment under N_2 atmosphere without phosphorus source) and benchmark commercial Pt/C were also studied. The respective current density was calculated based on the geometric area of utilized glassy carbon rotating disk electrode (GC-RDE, 0.196 cm^2). The linear sweep voltammetry (LSV) polarization curves in Fig. 3a designate the relatively inferior activity of Pt/C in alkaline HER with overpotential at 10 mA cm^{-2} (η_{10}) high as 67 mV (Fig. S7). In contrast, the PtNi NWs behave the ameliorative catalytic performance (η_{10}, 24 mV), owing to the Ni coupling and unique ultrafine one-dimensional nanowire features with high exposure of active sites. It is found that the PtNi NWs exhibits slightly higher HER activity than as-prepared PtNi NWs (without undergoing the heat treatment), which could be traced the morphologic evolution induced by heat treatment like Ni segregation (Fig. S8). Remarkably, the moderate P-doping further improves the alkaline HER performance by lowering the overpotentials (PtNiP-0.03 NWs and PtNiP-0.11 NWs), while the excessive P-doping causes the undesirable performance degeneration on account of the structural fragmentation (PtNiP-0.81 NWs). Among P-doped counterparts, PtNiP-0.11 NWs delivers the most excellent catalytic performance with lowest overpotential of only 12 mV at 10 mA cm^{-2} and 67 mV at 100 mA cm^{-2}, hinting the significant promotion effect of well-controlled P-doping on alkaline HER activity.

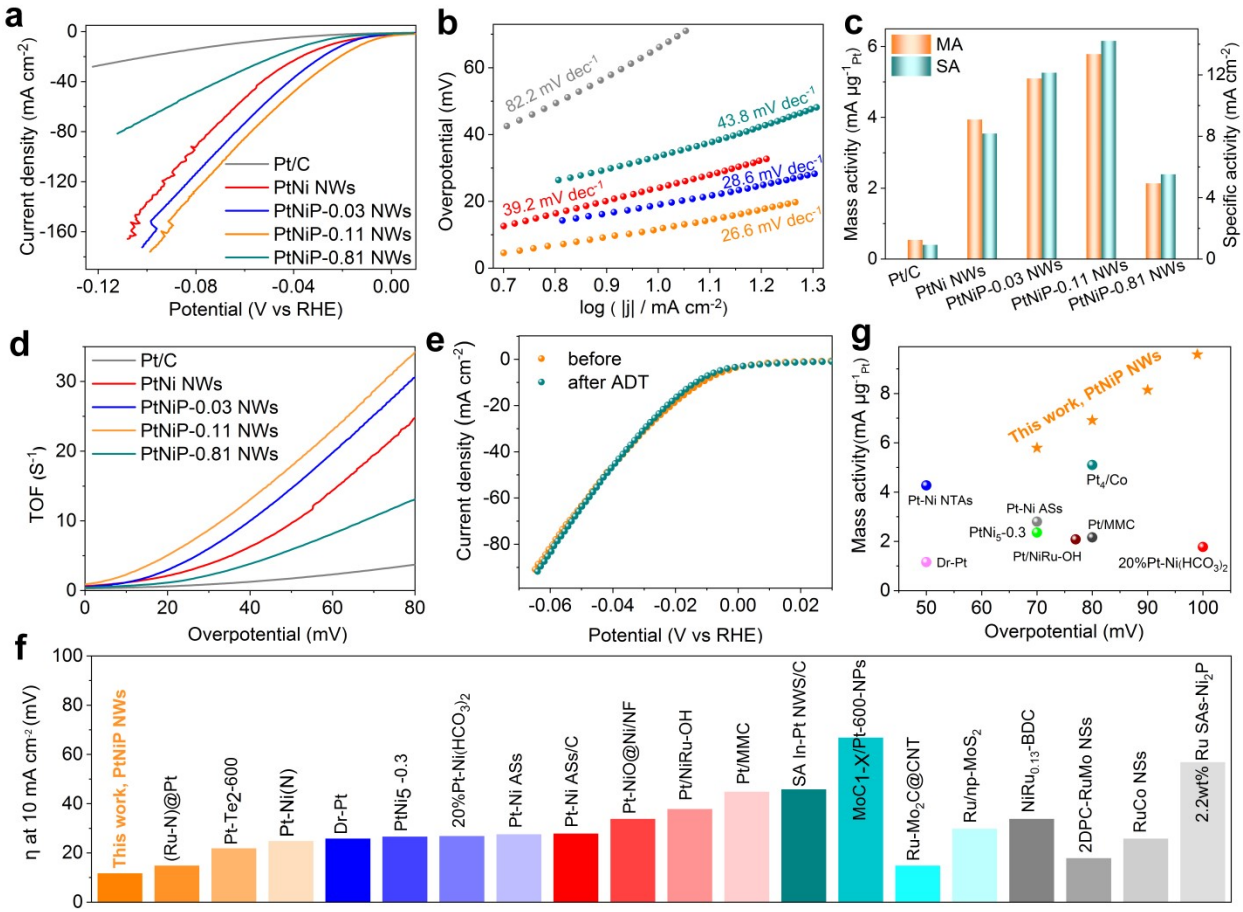

Fig. 3 Electrocatalytic HER performance of Pt/C, PtNi NWs and P-doped counterparts in N_2-saturated 1 M KOH electrolyte. (a) Polarization LSV curves with sweep rate of 5 mV s^{-1}. (b) The fitted Tafel plots. (c) Mass activity and specific activity at overpotentials of 70 mV. (d) TOF curves derived from polarization curves. (e) LSV curves of PtNiP-0.11 NWs before and after ADT *via* CV scanning between -0.1 V and 0.1 V *vs* RHE for 10000 cycles. (f) HER overpotentials contrast between PtNiP-0.11 NWs in this work and other state-of-the-art Pt/Ru-based catalysts in literatures. (g) Mass activity comparison between PtNiP-0.11 NWs in this work and other state-of-the-art Pt-based catalysts at corresponding overpotentials.

By fitting the polarization curves, Fig. 3b presents the Tafel plots for analyzing the HER kinetics. In line with the frustrated catalytic behavior, the Tafel slope of Pt/C is high as 82.2 mV dec^{-1}, suggesting the sluggish water dissociation (Volmer) step as rate-determining step (RDS) in alkaline medium. The Tafel slope of PtNi NWs equals to the lower 39.2 mV dec^{-1}, which

demonstrates that RDS switches from Volmer step to electrochemical desorption step and Ni introduction accelerates water dissociation kinetics.[35] The P-doping further lessens Tafel to 26.6 mV dec^{-1} for PtNiP-0.11 NWs, in which P atoms can promote both Volmer and desorption step. The extrapolation of Tafel plots proclaims the largest exchange current density at 3.51 mA cm^{-2}, corresponding to its optimal intrinsic activity (Fig. S9). Moreover, it is shown by Fig. 3c, S10 and S11 that PtNiP-0.11 NWs has the highest mass activity (5.8 A mg^{-1}_{Pt} at 70 mV) and specific activity (14.2 mA cm^{-2} at 70 mV) with notable improvement relative to un-doped counterparts. The turnover frequency (TOF) is also calculated to designate the intrinsic activity of diverse catalysts (Fig. 3d), where PtNiP-0.11 NWs holds the highest TOF of 28.6 s^{-1} at 70 mV, markedly outperforming the other electrocatalysts. On the other hand, catalyst stability was examined by accelerated durability test (ADT) *via* CV scan between -0.1 V and 0.1 V *vs* RHE for 10000 cycles. No obvious current density decay in polarization curves can be found for PtNiP-0.11 NWs after ADT (Fig. 3e). The TEM image after ADT also affirms the well-maintained nanowire structures of PtNiP-0.11 NWs (Fig. S12), in consistence with the reminded HER performance. Taking a broader view, the PtNiP-0.11 NWs behaves the outstanding catalytic HER activity in alkaline medium with small overpotential and high mass activity, overmatching the benchmark Pt/C and most of state-of-the-art noble-metal-based electrocatalysts (Fig. 3f-3g, Table S2-S3). These results together manifest the great potentials of PtNiP nanowires to replace and surpass Pt/C for practical HER application. In addition, we have further performed the etching treatment of PtNiP-0.11 NWs in acid to verify the function of Ni segregation on HER performance. It is clearly indicated by CV curves that acidic etching removed the surface Ni component to make Ni oxidation peak at around 1.4 V *vs* RHE, disappear (Fig. S13a). In consequence, the catalytic activity of PtNiP-0.11 NWs largely deteriorated, hinting the importance of Ni segregation on alkaline HER (Fig. S13b).

Mechanism insight into the boosted HER activity on P-doped PtNi NWs

We then turn into the underlying mechanism that contributed to the notably enhanced

alkaline HER performance of PtNi NWs by P-doping. The density functional theory (DFT) calculations were performed to gain a fundamental insight into the electronic structure-reactivity correlation *via* using Vienna Ab-initio Simulation Package. As illustrated in Fig. S14, the calculation model for Pt/C catalyst was set as a slab that consisted of four atomic layers of (4 × 4) supercell exposing *fcc* Pt (111) surface separated by 15 Å of vacuum space. The PtNi model was established by replacing several Pt atoms on Pt_3Ni (111) surface with segregational Ni cluster according to structure analysis above, while the configuration optimization resulted in the P position between bridge site and *hcp* hollow site for PtNiP model.[34] Accordingly, charge density difference (CDD) was analyzed to inspect the alteration of electronic structures by P-doping.[36, 37] As shown in Fig. 4a, the charge density distribution on Pt and Ni near to P was evidently reshaped by P heteroatom to make the surface more polarized that may induce more active sites. This echoes with XPS analysis that charge transfer interaction occurs between P and Pt/Ni metals, and could enhance the catalytic activity. Meanwhile, the electronic structure alteration was also confirmed by projected density of states (PDOS) of Pt sites in models (Fig. 4b). The P incorporation lowers the *d*-band center from -2.02 eV for PtNi to -2.06 eV for PtNiP. Therefore, *H adsorption is expected to be weakened so as to bring about a better HER activity on account of the slightly too strong *H binding on Pt site.[38]

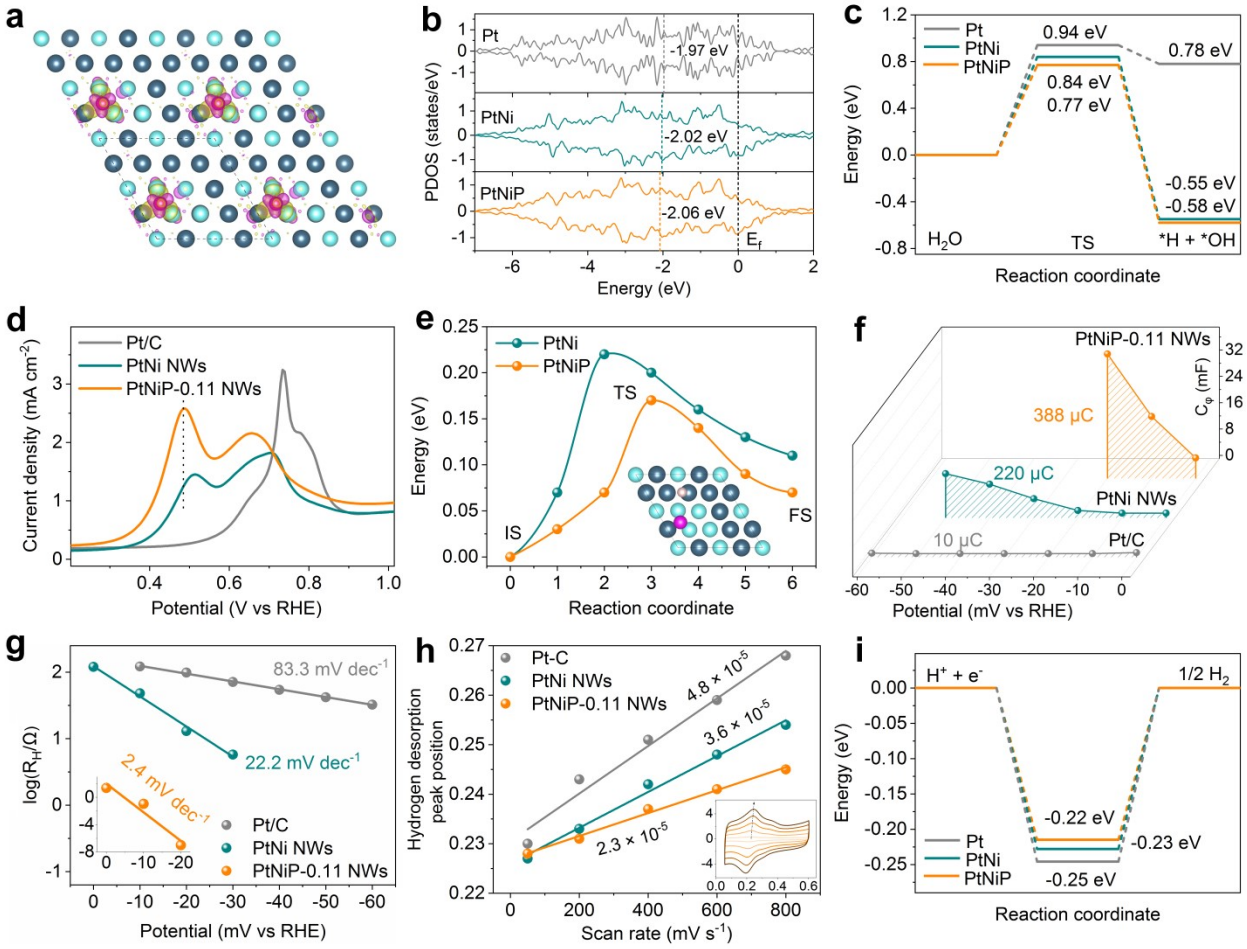

Fig. 4 Mechanism insights to the outstanding HER performance of P-doped PtNi NWs. (a) Charge density difference (CDD) analysis of PtNiP slab. (b) Calculated PDOS of Pt sites on Pt, PtNi, and PtNiP slabs. The *d*-band center and E_F are indicated. (c) Water dissociation kinetics on Pt, PtNi and PtNiP slabs. TS, transition state. (d) CO-stripping curves of Pt/C, PtNi NWs and PtNiP-0.11 NWs. (e) Calculated energy barriers of hydrogen migration across Pt-Ni interface on PtNi and PtNiP slabs. IS, initial state. FS, final state. The inset corresponds to TS configurations of PtNiP during hydrogen spillover. (f) Hydrogen adsorption pseudo-capacitance (C_φ) as function of potential and (g) EIS-derived Tafel plots for Pt/C, PtNi NWs and PtNiP-0.11 NWs obtained from EIS fitting. (h) Linear fitting of hydrogen desorption peak position *vs* scan rate in CV. The inset is the CV curves of PtNiP-0.11 NWs at varying scan rate from 50 mV s^{-1} to 800 mV s^{-1}, where *x*-axis and *y*-axis stand for potential (V *vs* RHE) and current density (mA cm^{-2}),

respectively. (i) Hydrogen adsorption free energy diagram on Pt, PtNi and PtNiP slabs.

Next, the energy profiles were calculated by dividing overall HER into three consecutive steps, i.e., water dissociation, interfacial hydrogen spillover, and H_2 desorption.[12] The optimized configurations of HER key species and some transition states on slabs are given in Fig. S15-S21. In the first step, Fig. 4c indicates that water dissociation on Pt (111) surface is sluggish with quite high dissociation energy and reaction barrier. The barrier can be significantly lowered by Ni alloying, where dissociation reaction directly occurs on Ni sites (Fig. S16). This is in accordance with the previous conclusions that Ni benefits to water dissociation step on Pt-based binary catalysts.[8] In contrast, the P incorporation further reduces the energy barrier from 0.84 eV to 0.77 eV, indicating the promotion effect of the P-doping on water dissociation step for PtNi. This effect could be directed to the good oxophilicity of P atoms functioning as sites to anchor and stabilize OH^- generated from water dissociation.[39, 40] In the optimized configuration, the preferential binding of OH^- in P sites is witnessed as well on PtNiP slab (Fig. S17). The proposal is further supported by CO stripping curves (Fig. 4d and S22), where PtNiP holds the earliest onset potential for oxidative removal of CO and therefore the strongest OH^- binding,[35] in comparison to PtNi catalyst. Besides, the more polarized and unsymmetrical structure of H_2O molecule adsorbed on PtNiP catalyst again reflects the corresponding facile water dissociation kinetics (Fig. S23).

More importantly in the second step, the hydrogen spillover across the Pt-Ni interface to reach Pt site also requires to be promoted for better HER activity in phase-separated PtNi NWs (Fig. 1e-1f). This is reasonable because water dissociation occurs on Ni phase, and much stronger *H adsorption on Ni site than that on Pt makes Pt the more suitable site for hydrogen combination and H_2 releasing. However, for general Pt-based hybrid catalysts, challenges confront the interfacial hydrogen migration that is not thermodynamically or kinetically favored.[18] To examine whether P-doping can boost this step, hydrogen migration kinetics difference is then compared between PtNi and PtNiP catalysts.[41] It is clearly demonstrated by Fig.

4e that PtNiP behaves a smaller energy barrier (0.17 eV) than that on PtNi slab (0.22 eV). In the presence of adsorbed OH^- on slab from water dissociation, the migration barrier is relatively lower on PtNiP as well (Fig. S24). Therefore, P-doping is discovered to kinetically enhance the interfacial hydrogen spillover step on hybrid catalyst, which could arise from the optimization of electronic structures by P heteroatoms. According to the mechanistic investigations from Qu *et al.*, the accelerated migration kinetics on PtNiP could also be explained from aspects of work function ($\Delta\Phi$).[16] As P-doping might preferentially occur on more active Ni (Fig. 2), the higher $\Delta\Phi$ of nickel phosphide in contrast to Ni would reduce $\Delta\Phi$ difference between Ni and Pt,[42-44] leading to the decreased interfacial charge accumulation and promoted hydrogen migration across Pt-Ni interface.[16, 45]

On the other hand, experimentally, EIS measurements were performed to monitor the local *H concentration under HER conditions so as to evaluate the thermodynamic driving force for hydrogen spillover on different catalysts (Fig. S25-S27). The potential-dependent Nyquist plots were fitted based on a typical double-parallel equivalent circuit model (Fig. S28 and Table S4).[16] The R_s represents the solution resistance, which is similar for all catalysts or applied potentials. The first parallel components (T and R_{CT}) describe the charge-transfer kinetics. In most case, the R_{CT} gradually decreases with overpotential rising, hinting the enhanced HER charge transfer kinetics by applying potentials. The second parallel components reflect the hydrogen adsorption behaviors comprised of hydrogen adsorption pseudo-capacitance (C_φ) and resistance (R_H). As shown in Table S4, C_φ gradually increases with applied potentials, and peaks (or slightly declines) after reaching saturated hydrogen adsorption, while R_H continuously decreases. Notably, integration of C_φ *vs* potential within saturation range determines the hydrogen adsorption charge (Q_H), corresponding to the local *H coverage or concentration. It is exhibited by Fig. 4f that PtNiP-0.11 NWs possesses much higher *H coverage (Q_H = 388 μC) in comparison to that on PtNi NWs surface (Q_H = 200 μC). In consequence, the higher concentration of *H on P-doped nanowires caused by the enhanced water dissociation (Fig. 4c), can offer a larger thermodynamic driving force to motivate the interfacial hydrogen spillover process.[18] The EIS-derived Tafel

analysis by plotting log R_H *vs* potential in Fig. 4g, also gives the markedly lower hydrogen-adsorption-resistance-involved Tafel slope of PtNiP (4.3 mV dec^{-1}) than that of PtNi (22.2 mV dec^{-1}), which describes the boosted hydrogen adsorption kinetics and more facile hydrogen spillover process on PtNiP-0.11 NWs. In addition, the sensitivity of hydrogen desorption peak position to scan rate during CV investigations can be used as a descriptor to reflect hydrogen desorption kinetics and evidence the occurrence of hydrogen spillover.[15, 45] As Fig. 4h and S29 display, the hydrogen desorption peak shifts positively with scan rate increasing for all catalysts, among which PtNiP-0.11 NWs possesses lowest slope value. It is consequently indicated that the facile kinetics of hydrogen desorption on PtNiP-0.11 NWs can be linked to the strengthened hydrogen spillover behavior. Based on these theoretical and experimental results, we can conclude that P incorporation significantly promotes the interfacial hydrogen spillover behavior on phase-separated PtNi binary catalyst through improving both thermodynamic and kinetic driving force.

Finally, in the H_2 desorption step, the ΔG_H was also calculated as a descriptor to evaluate the intrinsic HER activity.[38] It is expected that P-doping can further reduce *H binding strength on Pt site to benefit the H_2 releasing. In this regarded, Fig. 4i demonstrates PtNiP behaves the weakest hydrogen adsorption compared to Pt and PtNi catalyst, in accordance with its lowest *d*-band center in Fig. 4b and more facile H_2 releasing process to realize a better HER performance. On all accounts, as results of these mechanism insights, the P incorporation can modulate electronic structure of PtNi NWs, and significantly promote interfacial hydrogen spillover by increasing *H coverage and reducing migration barrier. These result in the significantly enhanced *H supply on Pt sites, which together with the optimized slightly ΔG_H, ultimately improve overall HER activity.

Conclusion

In summary, we have demonstrated that P-doping can thermodynamically and kinetically boost the hydrogen migration to increase *H supply on Pt sites for promotion of alkaline HER on Pt-

based binary catalyst. Through a vapor phase method, P heteroatoms were effectively incorporated to ultrafine PtNi NWs. XPS together with theoretical CDD analysis evidenced the charge transfer interaction between P and metal atoms on NWs, enabling the modulation of electronic structures and optimization of *d*-band center. As consequences of structure-reactivity sensitivity, water dissociation was firstly boosted on PtNiP NWs to produce more *H, due to the increased H_2O polarization, and OH^- stabilization by P sites. In particular, theoretical simulations revealed the notably reduced kinetic barrier of hydrogen migration across Pt-Ni interface in the presence of P heteroatoms. Experimentally, electrochemical analysis confirmed the much higher *H coverage on PtNiP NWs and corresponding smaller hydrogen absorption resistance, which reflected the higher thermodynamics driving force for interfacial hydrogen migration. As results of enhanced *H supply on Pt sites from promoted hydrogen spillover, and the further optimized ΔG_H, PtNiP NWs delivered an impressive alkaline HER activity surpassing most of state-of-the-art electrocatalysts, with η_{10} of 12 mV, Tafel slope of 26.6 mV dec^{-1}, and mass activity of 5.8 A mg^{-1}_{Pt} at 70 mV.

Authorship Contributions

Wenchuan Lai: Conceptualization, Methodology, Investigation, Formal analysis, Data Curation, Funding acquisition, Writing - original draft. **Penglin Yu**: Methodology, Investigation, Formal analysis. **Lei Gao**: Investigation. **Zhilong Yang**: Investigation. **Bingling He**: Conceptualization, Methodology, Resources. **Hongwen Huang**: Conceptualization, Methodology, Funding acquisition, Writing - review & editing, Supervision, Project administration.

Declaration of Competing Interest

The authors declare that they have no known competing financial interests or personal relationships that could have appeared to influence the work reported in this paper.

Acknowledgements

This work was supported by the National Key Research and Development Program of China (No. 2021YFA1502000), NSFC (No. U2032149 and 22102052), the Science and Technology Innovation Program of Hunan Province (No. 2021RC3065 and 2021RC2053), Hunan Provincial Natural Science Foundation of China (No. 2020JJ2001), Shenzhen Science and Technology Program (No. JCYJ20210324120800002).

References

1. J. Zhu, L. Hu, P. Zhao, L. Y. S. Lee and K.-Y. Wong, *Chem. Rev.*, 2020, **120**, 851-918.
2. H. Wang, W. Fu, X. Yang, Z. Huang, J. Li, H. Zhang and Y. Wang, *J. Mater. Chem. A*, 2020, **8**, 6926-6956.
3. S. Jiao, X. Fu, S. Wang and Y. Zhao, *Energy Environ. Sci.*, 2021, **14**, 1722-1770.
4. J. Guan, X. Bai and T. Tang, *Nano Res.*, 2022, **15**, 818-837.
5. L. Gao, Z. Yang, T. Sun, X. Tan, W. Lai, M. Li, J. Kim, Y.-F. Lu, S.-I. Choi, W. Zhang, C. Ma, S. C. Smith, Y.-G. Zhou and H. Huang, *Adv. Energy Mater.*, 2022, **12**, 2103943.
6. G. H. Gu, J. Lim, C. Wan, T. Cheng, H. Pu, S. Kim, J. Noh, C. Choi, J. Kim, W. A. Goddard, X. Duan and Y. Jung, *J. Am. Chem. Soc.*, 2021, **143**, 5355-5363.
7. Y. Z. Wang, M. Yang, Y.-M. Ding, N.-W. Li and L. Yu, *Adv. Funct. Mater.*, 2022, **32**, 2108681.
8. R. Subbaraman, D. Tripkovic, D. Strmcnik, K.-C. Chang, M. Uchimura, P. Paulikas Arvydas, V. Stamenkovic and M. Markovic Nenad, *Science*, 2011, **334**, 1256-1260.
9. R. Subbaraman, D. Tripkovic, K.-C. Chang, D. Strmcnik, A. P. Paulikas, P. Hirunsit, M. Chan, J. Greeley, V. Stamenkovic and N. M. Markovic, *Nat. Mater.*, 2012, **11**, 550-557.
10. J. Ding, Y. Ji, Y. Li and G. Hong, *Nano Lett.*, 2021, **21**, 9381-9387.
11. C.-T. Dinh, A. Jain, F. P. G. de Arquer, P. De Luna, J. Li, N. Wang, X. Zheng, J. Cai, B. Z. Gregory, O. Voznyy, B. Zhang, M. Liu, D. Sinton, E. J. Crumlin and E. H. Sargent, *Nat. Energy*, 2019, **4**, 107-114.
12. H. Q. Fu, M. Zhou, P. F. Liu, P. Liu, H. Yin, K. Z. Sun, H. G. Yang, M. Al-Mamun, P. Hu,

H. F. Wang and H. Zhao, *J. Am. Chem. Soc.*, 2022, **144**, 6028-6039.

13. P. Li, G. Zhao, P. Cui, N. Cheng, M. Lao, X. Xu, S. X. Dou and W. Sun, *Nano Energy*, 2021, **83**, 105850.
14. M. Xiong, Z. Gao and Y. Qin, *ACS Catal.*, 2021, **11**, 3159-3172.
15. J. Dai, Y. Zhu, Y. Chen, X. Wen, M. Long, X. Wu, Z. Hu, D. Guan, X. Wang, C. Zhou, Q. Lin, Y. Sun, S. C. Weng, H. Wang, W. Zhou and Z. Shao, *Nat Commun*, 2022, **13**, 1189.
16. J. Li, J. Hu, M. Zhang, W. Gou, S. Zhang, Z. Chen, Y. Qu and Y. Ma, *Nat Commun*, 2021, **12**, 3502.
17. T. Kim, S. B. Roy, S. Moon, S. Yoo, H. Choi, V. G. Parale, Y. Kim, J. Lee, S. C. Jun, K. Kang, S.-H. Chun, K. Kanamori and H.-H. Park, *ACS Nano*, 2022, **16**, 1625-1638.
18. J. Li, H.-X. Liu, W. Gou, M. Zhang, Z. Xia, S. Zhang, C.-R. Chang, Y. Ma and Y. Qu, *Energy Environ. Sci.*, 2019, **12**, 2298-2304.
19. J. Wei, S.-N. Qin, J.-L. Liu, X.-Y. Ruan, Z. Guan, H. Yan, D.-Y. Wei, H. Zhang, J. Cheng, H. Xu, Z.-Q. Tian and J.-F. Li, *Angew. Chem. Int. Ed.*, 2020, **59**, 10343-10347.
20. Y. Zhu, P. Tian, H. Jiang, J. Mu, L. Meng, X. Su, Y. Wang, Y. Lin, Y. Zhu, L. Song and C. Li, *CCS Chem.*, 2021, **3**, 2539-2547.
21. B. Jiang, L. Yang, F. Liao, M. Sheng, H. Zhao, H. Lin and M. Shao, *Nano Res.*, 2017, **10**, 1749-1755.
22. E. V. Miu, J. R. McKone and G. Mpourmpakis, *J. Am. Chem. Soc.*, 2022, **144**, 6420-6433.
23. H. Tan, B. Tang, Y. Lu, Q. Ji, L. Lv, H. Duan, N. Li, Y. Wang, S. Feng, Z. Li, C. Wang, F. Hu, Z. Sun and W. Yan, *Nat. Commun.*, 2022, **13**, 2024.
24. J. Park, S. Lee, H. E. Kim, A. Cho, S. Kim, Y. Ye, J. W. Han, H. Lee, J. H. Jang and J. Lee, *Angew. Chem. Int. Ed.*, 2019, **58**, 16038-16042.
25. W. Tian, Y. Wang, W. Fu, J. Su, H. Zhang and Y. Wang, *J. Mater. Chem. A*, 2020, **8**, 20463-20473.
26. H. Du, R.-M. Kong, X. Guo, F. Qu and J. Li, *Nanoscale*, 2018, **10**, 21617-21624.
27. L. Chen, L. Lu, H. Zhu, Y. Chen, Y. Huang, Y. Li and L. Wang, *Nat. Commun.*, 2017, **8**,

14136.

28. P. Wang, X. Zhang, J. Zhang, S. Wan, S. Guo, G. Lu, J. Yao and X. Huang, *Nat. Commun.*, 2017, **8**, 14580.

29. L. Gao, T. Sun, X. Tan, M. Liu, F. Xue, B. Wang, J. Zhang, Y.-F. Lu, C. Ma, H. Tian, S. Yang, S. C. Smith and H. Huang, *Appl. Catal. B: Environ.*, 2022, **303**, 120918.

30. L. Gao, X. Li, Z. Yao, H. Bai, Y. Lu, C. Ma, S. Lu, Z. Peng, J. Yang, A. Pan and H. Huang, *J. Am. Chem. Soc.*, 2019, **141**, 18083-18090.

31. L. Li, T. Zhang, J. Yan, X. Cai and S. Liu, *Small*, 2017, **13**, 1700441.

32. B. Ma, Z. Yang, Y. Chen and Z. Yuan, *Nano Res.*, 2019, **12**, 375-380.

33. J. Liu, Z. Wang, J. Li, L. Cao, Z. Lu and D. Zhu, *Small*, 2020, **16**, 1905738.

34. Y. Zhao, X. Wang, G. Cheng and W. Luo, *ACS Catal.*, 2020, **10**, 11751-11757.

35. T. Tang, L. Ding, Z.-C. Yao, H.-R. Pan, J.-S. Hu and L.-J. Wan, *Adv. Funct. Mater.*, 2022, **32**, 2107479.

36. W. Song, K. Xie, J. Wang, Y. Guo, C. He and L. Fu, *Phys. Chem. Chem. Phys.*, 2021, **23**, 10418-10428.

37. D. Chen, Z. Chen, X. Zhang, Z. Lu, S. Xiao, B. Xiao and C. V. Singh, *J. Energy Chem.*, 2021, **52**, 155-162.

38. S. Jiao, X. Fu and H. Huang, *Adv. Funct. Mater.*, 2021, **32**, 2107651.

39. Z. Pu, I. S. Amiinu, Z. Kou, W. Li and S. Mu, *Angew. Chem. Int. Ed.*, 2017, **56**, 11559-11564.

40. A. Hirsch and F. Hauke, *Angew. Chem. Int. Ed.*, 2018, **57**, 4338-4354.

41. B. Jiang, Z. Tang, F. Liao, H. Lin, S. Lu, Y. Li and M. Shao, *J. Mater. Chem. A*, 2017, **5**, 21903-21908.

42. Y. Li and D. Y. Li, *J. Appl. Phys.*, 2004, **95**, 7961-7965.

43. D. Dai, L. Wang, N. Xiao, S. Li, H. Xu, S. Liu, B. Xu, D. Lv, Y. Gao, W. Song, L. Ge and J. Liu, *Appl. Catal. B: Environ.*, 2018, **233**, 194-201.

44. R. K. Khisamov, I. M. Safarov, R. R. Mulyukov and Y. M. Yumaguzin, *Phys. Solid State*,

2013, **55**, 1-4.

45. J. Li, Y. Tan, M. Zhang, W. Gou, S. Zhang, Y. Ma, J. Hu and Y. Qu, *ACS Energy Lett.*, 2022, **7**, 1330-1337.